Separation and Purification Technology 345 (2024) 127348

Contents lists available at ScienceDirect

Separation and Purification Technology

journal homepage: www.elsevier.com/locate/seppur

Highly efficient catalytic oxidation of toluene by amorphous/microcrystalline mixed-phase MnO_2

Jungang Zhao [a,b], Caiting Li [a,b,*], Xuan Liu [a,b], Shanhong Li [a,b], Youcai Zhu [c], Le Huang [a,b], Kuang Yang [a,b], Ziang Zhang [a,b], Ying Zhang [a,b], Qi Huang [a,b]

[a] *College of Environmental Science and Engineering, Hunan University, Changsha 410082, PR China*
[b] *Key Laboratory of Environmental Biology and Pollution Control (Hunan University), Ministry of Education, Changsha 410082, PR China*
[c] *Shandong Key Laboratory of Environmental Processes and Health, School of Environmental Science and Engineering, Shandong University, Qingdao 266237, PR China*

ARTICLE INFO

Editor: Jorge Bedia

Keywords:
Catalytic oxidation
Toluene
Amorphous
Manganese oxide

ABSTRACT

Amorphous transition metal oxides exhibit considerable potential in the catalytic oxidation of volatile organic compounds (VOCs) owing to their distinctive surface properties. In this study, we achieved the modulation of the crystalline structure of manganese oxides by employing various C_3 alcohols (alcohols with three carbons) with distinct hydroxyl types during the reduction process with potassium permanganate. Subsequently, a series of characterization techniques were employed to assess the catalytic performance of the prepared MnO_2 in the oxidation of toluene. Notably, the MnO_2-G obtained from glycerol presented excellent catalytic activity ($T_{90} = 219\ ^\circ C$), stability, and water resistance. The unique amorphous/microcrystalline state of MnO_2-G exposed more phase boundaries, and the unsaturated coordination structure facilitated the generation of additional defective sites, favoring the adsorption and activation of oxygen. Furthermore, the mixed-crystalline state induced the elevated Mn^{3+} content on the surface of MnO_2-G, leading to elongation of the Mn-O bond due to the pronounced Jahn-Teller effect of Mn^{3+}. Consequently, the synergistic effects of the mixed crystalline state contributed to the efficient catalytic oxidation of toluene at relatively low temperatures. Additionally, the conversion pathway of toluene on MnO_2-G was further revealed by in situ DRIFTS.

1. Introduction

VOCs are another air pollutant that has been increasingly emphasized after $PM_{2.5}$, sulfur dioxide, and nitrogen oxides, including alkanes, olefins, and aromatic hydrocarbons [1]. Among them, hydrocarbons with benzene rings are often highly toxic, irritating, and strongly carcinogenic, and can pose a serious risk to the human respiratory and immune systems [2–5]. Moreover, VOCs are now the critical precursors for the formation of O_3 and photochemical smog, posing a serious threat to the environment [6,7]. There is a great deal of urgency in the management of VOCs. Among many VOCs treatment methods (e.g. adsorption, plasma, photocatalysis, catalytic oxidation et al), catalytic oxidation technology is currently one of the most mainstream technologies owing to low cost, great efficiency, and without secondary pollution [1,8,9]. Catalyst is the key to determining the efficiency of catalytic oxidation treatment, usually involving precious metal and transition metal catalysts [10,11]. Although noble metal catalysts have naturally high catalytic activity, their scarcity, high price, ease of sintering, and poor resistance to toxicity limit their widespread application [12–14]. On the other hand, transition metal oxide catalysts have been increasingly investigated due to their relatively high activity, low price, and high resistance to toxicity [15–17].

Currently, researchers have conducted thorough investigations into the structure-effect relationship encompassing the crystal type, exposed crystal surface, and morphology of crystalline transition metal oxides in relation to catalytic activity [18,19]. Compared with crystalline catalysts, amorphous or partially crystalline catalysts are prone to generate a large number of unsaturated coordination sites and oxygen vacancies due to the disordered arrangement and the loose bonding between the internal atoms. This characteristic endows amorphous or mixed-crystalline transition metal oxides with abundant active sites and a wealth of reactive oxygen species, thereby significantly enhancing their catalytic activity. Dong et al. employed an impregnation-pyrolysis method to anchor amorphous Co_3O_4 particles onto biochar. The defect-rich Co_3O_4 facilitated the activation of PMS, significantly enhancing the performance of the removal of sulfamethoxazole from

---

* Corresponding author at: College of Environmental Science and Engineering, Hunan University, Changsha 410082, PR China.
E-mail address: ctli@hnu.edu.cn (C. Li).

https://doi.org/10.1016/j.seppur.2024.127348
Received 4 February 2024; Received in revised form 26 March 2024; Accepted 2 April 2024

water. [20]. Lee et al. prepared amorphous CeO_2-TiO_2 using the H_2O_2-modified sol–gel method, and its redox properties were significantly improved compared to crystalline CeO_2-TiO_2 [21]. In another study, Huang et al. synthesized amorphous FeO_x-$Mn_{0.1}O_y$ through Mn doping, which exhibited significant NO and O_2 adsorption enhancement and promoted selective reduction of ammonia at low temperatures [22]. Although an increasing number of materials with hybrid amorphous structures have been applied in various catalytic reactions in recent years, there is still relatively limited research in the catalytic removal of VOCs.

MnO_2 is one of the most researched materials for the catalytic oxidation of VOCs owing to its wide range of sources, low price, variable valence, and high oxygen storage capacity [23–26]. Among the various crystalline forms of MnO_2, including α-, β-, γ-, and δ-MnO_2, it is noteworthy that δ-MnO_2 and α-MnO_2 usually possess the most outstanding catalytic oxidation performance [27,28]. However, recent studies suggest that amorphous MnO_2 may exhibit superior catalytic performance compared to crystalline MnO_2. Zhuang's group demonstrated that the amorphous MnO_2 nanostructure can carry highly reactive lattice oxygen, facilitating the catalytic oxidation of 5-hydroxymethylfurfural to 2,5-furan dicarboxylic acid (FDCA). The observed rate of FDCA formation for the amorphous MnO_2 is 8.2 times greater than that of crystalline MnO_2 [29]. For soot oxidation, Liu et al. provided evidence that amorphous MnO_2 prepared using the colloidal solution combustion method had more surface oxygen species and improved low-temperature reducibility than crystalline MnO_2 [30]. Furthermore, Liu et al. synthesized partially crystalline MnO_2 using a gradient crystallization method. The specific procedure was to reduce $KMnO_4$ with glucose to obtain amorphous MnO_2, followed by a secondary hydrothermal heating process to enhance crystallinity. The obtained mixed-crystalline MnO_2 exhibited superior catalytic combustion performance for VOCs. This is attributed to the coexistence of amorphous and crystalline structures that could synergize to provide the catalysts with stronger oxygen supply capacity and more Mn^{4+} [31]. Despite the attractiveness of the amorphous strategy, reports on the facile preparation of MnO_2 with crystalline/amorphous states are still relatively limited. Moreover, it is necessary to deeply investigate the mechanism of catalytic combustion of VOCs by partially crystalline MnO_2.

Herein, MnO_2 catalysts with different crystal types and surface properties were prepared by reducing $KMnO_4$ with C_3-alcohols containing different numbers of hydroxyl groups. Among them, MnO_2-G obtained from glycerol presented the optimal catalytic performance. XRD and HRTEM analyses showed that MnO_2-G consists of abundant mixed amorphous and microcrystalline structures. Raman and XPS illustrated that the hybrid crystal structure facilitates the weakening of the Mn-O bond and generates more oxygen vacancies. Furthermore, the significant enhancement of the MnO_2-G 's redox capacity and surface lattice oxygen activation was demonstrated by H_2-TPR and O_2-TPD. And the isotope labeling test proved that both chemisorbed and lattice oxygen are involved in the toluene oxidation process. Meanwhile, the conversion pathway of toluene on the MnO_2-G surface was examined by in situ DRIFTS. Moreover, MnO_2-G exhibited excellent stability, water tolerance, and operational flexibility.

2. Experimental

2.1. Preparation of catalyst

The redox-precipitation method was used to synthesize different MnO_2 samples. Specifically, 35 mL deionized water was used to dissolve 0.3 mol of C_3 alcohol (1-propanol, isopropanol, 1,2-propylene glycol, 1,3-propylene glycol, and glycerol). Then, 30 mL deionized water was used to dissolve 0.01 mol $KMnO_4$, and the mixture was ultrasound for 15 min. Thereafter, the $KMnO_4$ solution was added dropwise into the C_3 alcohol solution at 60 °C with vigorous stirring and kept for 6 h. Subsequently, the precipitated product was centrifuged and washed three times alternately with deionized water and ethanol. Finally, the as-synthesized samples were dried in an oven at 80 °C overnight, followed by calcination in a tubular furnace at 400 °C under an air atmosphere for 4 h to obtain powder catalysts. The catalysts prepared using 1-propanol, isopropanol, 1,2-propylene glycol, 1,3-propylene glycol, and glycerol as reducing agents were sequentially named MnO_2-P, MnO_2-I, MnO_2-1,2P, MnO_2-1,3P, and MnO_2-G.

2.2. Characterizations of catalyst

The samples were comprehensively characterized through a wide range of analytical techniques. X-ray diffraction (XRD) analysis was conducted utilizing a Rigaku Smart Lab power diffractometer equipped with Cu Kα radiation, and the scan rate was set at 5°/min. X-ray photoelectron spectroscopy (XPS) was employed to analyze the valence state and electron transfer of the catalysts. Nitrogen adsorption and desorption isotherms were documented employing a Quantachrome Nova 4000e instrument. The specific surface area (S_{BET}) and pore volume (V_p) were determined via the Brunauer-Emmett-Teller (BET) and Barret-Joyner-Halenda (BJH) methods. A HOBIBA spectrometer with an excitation wavelength of 532 nm was used to investigate the Raman vibrational characteristics of the catalysts. Morphology and structure examination involved scanning electron microscopy (SEM, TESCAN MIRA4) and transmission electron microscopy (TEM, FEI Tecnai G2 F20). H_2 temperature-programmed reduction (H_2-TPR) experiments were performed on a Micromeritics AutoChem II 2920 instrument. The catalysts were pretreated in a helium stream (50 mL/min) at 300 °C for 60 min, followed by temperature ramping to 800 °C in a 5 % H_2/Ar flow (50 mL/min), while recording the thermal conductivity detector (TCD) signal. The hydrogen consumption of a series of CuO standard samples and their reduction peak area were used as benchmarks to calculate the hydrogen consumption corresponding to the reduction peak area of the test sample [32]. Similarly, O_2 temperature-programmed desorption (O_2-TPD) experiments were performed with pretreated catalysts using a helium gas stream (50 mL/min) from 50 to 800 °C at a rate of 10 °C /min. In situ diffuse reflectance infrared Fourier transform spectroscopy (in situ DRIFTS) analyses were performed using a Thermo Fisher Nicolet 6700 FTIR spectrometer. The samples underwent pretreatment in a helium flow at 230 °C for 1 h to eliminate surface water and physically adsorbed oxygen. Subsequently, 600 ppm toluene was injected into the in situ cell balanced with synthetic air. The $^{18}O_2$ temperature-programmed surface reaction ($^{18}O_2$-TPSR) was conducted for isotopic labeling tests. The samples were first pretreated at 300 °C for 30 min under He atmosphere to remove adsorbed oxygen on the catalyst surface. The samples were then cooled to 60 °C, followed by the introduction of C_7H_8/He gas and maintained for 30 min. After purging with He and stabilizing the baseline for mass spectrometry, the atmosphere was switched to 3 %$^{18}O_2$ and the temperature was heated to 400 °C at a ramp rate of 10 °C/min. The exit gas was analyzed online using a mass spectrometer (AutoChem 2950 HP).

2.3. Catalytic activity measurement

All experiments assessing the catalytic oxidation performance of MnO_2 catalysts for toluene oxidation were conducted within a continuous-flow fixed-bed reactor. A total of 100 mg of catalyst (40–80 mesh) was loaded into the system. The inlet gas flow rate was set at 50 $mL{\cdot}min^{-1}$ with a composition of 600 ppm toluene or 500 ppm chlorobenzene, 20 vol% oxygen, and nitrogen as the balance gas. This corresponds to a weight hourly space velocity (WHSV) of 30,000 $mL{\cdot}h^{-1}{\cdot}g^{-1}$. To investigate the influence of WHSV on the catalytic oxidation of toluene, the amount of catalyst was adjusted to WHSV = 60,000 and 120,000 $mL{\cdot}h^{-1}{\cdot}g^{-1}$. Moreover, the impact of water vapor on the toluene oxidation performance of the catalyst was investigated by introducing varying concentrations, specifically 2.5, 5, 10, 15, and 20 vol%, of water vapor to the reaction process. Toluene and CO_2

concentration were continuously measured employing an online gas chromatograph featuring a flame ionization detector (GC-2017C, Shimadzu) and a CO_2 detector (PGA 650, Phymetrix).

Toluene conversion (X, %) and CO_2 yield were calculated using the following equations:

$$X = \frac{[C_7H_8]_{in} - [C_7H_8]_{out}}{[C_7H_8]_{in}} \times 100\% \tag{1}$$

$$CO_2\ Yield = \frac{[CO_2]_{out}}{7 \times [C_7H_8]_{in}} \times 100\% \tag{2}$$

where $[C_7H_8]_{in}$ and $[C_7H_8]_{out}$ denote the toluene concentration in the feed gas and at the reactor outlet, respectively; $[CO_2]_{out}$ represents the observed CO_2 concentration at the reactor outlet.

The reaction rate (r, $mol \cdot s^{-1} \cdot g^{-1}$) of the samples was computed using the following formula:

$$r = \frac{X \times 600 \times 10^{-6} \times V}{22.4 \times 60 \times 1000 \times m} \tag{3}$$

where V represents the total gas flow rate ($mL \cdot min^{-1}$) and m is the mass (g) of the tested catalyst.

To assess the catalytic activity more effectively, the apparent activation energy (Ea, $kJ \cdot mol^{-1}$) was determined using the Arrhenius formula.

$$r = k_0 \times e^{-E_a/RT} \tag{4}$$

3. Results and discussion

3.1. *Structures and morphology*

To determine the crystal structure of these synthesized MnO_2, the samples were subjected to XRD tests, and the analytical results are shown in Fig. 1**a**. In the case of the MnO_2-P catalyst, diffraction peaks at 12.78° and 37.52° were identified, associated with the crystal planes (1 1 0) and (2 1 1) of α-MnO_2 (PDF#44–0141). The MnO_2-I exhibited a mixed crystalline phase, its diffraction peak of 37.52° corresponds to the (2 1 1) crystallographic plane of α-MnO_2, while the diffraction peaks at 12.55° and 25.25° are in agreement with the crystallographic planes (0 0 1) and (0 0 2) of δ-MnO_2 (PDF#80–1098). The XRD spectra of MnO_2-1,2P, MnO_2-1,3P, and MnO_2-G also displayed characteristic diffraction peaks of α-MnO_2. It is notable that MnO_2-G exhibits a single diffraction peak at 37.52° with low intensity, indicating a lower overall crystallinity compared to other MnO_2 samples, suggesting the possible presence of an amorphous structure [29]. Additionally, the broader XRD diffraction peak of MnO_2-G was likely attributed to its smaller grain size [31]. The amorphous characteristics and diminutive grain size contributed to the formation of dangling bonds or increased exposure of grain boundaries, consequently leading to the generation of more defects and facilitating catalytic oxidation reactions [33].

Fig. 1**(b-c)** shows the adsorption and desorption isotherm curves as well as the BJH pore size distribution of MnO_2 catalysts prepared by the reduction of $KMnO_4$ with various C_3 alcohols. All the samples exhibit type IV isotherms. MnO_2-P and MnO_2-1,2P feature H3-type hysteresis loops, MnO_2-1,3P displays H1 hysteresis, and the MnO_2-I and MnO_2-G are characterized by H4-type hysteresis loops, suggesting that different types of particle stacking exist for these catalysts [24,34]. Combining the pore size distributions in Table 1 reveals evident mesoporous structures in these MnO_2 samples. In comparison to other MnO_2, MnO_2-G demonstrates a notably narrower pore size distribution, featuring an average pore size of 6.65 nm. Furthermore, its pore volume (0.38 $cm^3 \cdot g^{-1}$) is the second smallest of all manganese dioxide catalysts, higher only than that of MnO_2-I. Additionally, MnO_2-G exhibits a specific surface area of 194.10 $m^2 \cdot g^{-1}$, surpassing only that of MnO_2-I (49.34 $m^2 \cdot g^{-1}$) but falling below those of MnO_2-P (206.25 $m^2 \cdot g^{-1}$), MnO_2-1,2P (205.38 $m^2 \cdot g^{-1}$), and MnO_2-1,3P (218.57 $m^2 \cdot g^{-1}$). Despite not having a superior surface area and pore volume, MnO_2-G exhibits significantly better toluene and chlorobenzene oxidation performance compared to other MnO_2 catalysts (Fig. 5**a** and **Fig. S3**). This indicates that the variations in catalytic performance are not primarily attributable to differences in specific surface area and pore volume. The micromorphology of these MnO_2 catalysts was investigated using SEM and TEM, as depicted in Fig. 2. MnO_2-P exhibits a characteristic rod-like structure of α-MnO_2 with an average diameter of around 26.20 nm. The lattice fringe spacing of 0.339 nm corresponds to the MnO_2 (2 2 0) crystal face. MnO_2-I is particle-shaped with an average particle size of 70.23 nm. According to XRD results, MnO_2-I is of a mixed crystal type, and HRTEM reveals lattice fringes with distances of 0.306 nm and 0.253 nm, corresponding to the α-MnO_2 (3 1 0) and δ-MnO_2 (2 0 0) crystal faces, respectively (Fig. 2**b$_3$**). MnO_2-1,2P and MnO_2-1,3P exhibit dense particle and layered structures, with average particle sizes of 35.81 and 82.68 nm, respectively. Similar to the structure of MnO_2-1,2P, MnO_2-G is composed of

Table 1
The textural properties of MnO_2 catalysts prepared by different C_3 alcohols.

Catalyst	S_{BET} ($m^2 \cdot g^{-1}$)[a]	V_p ($cc \cdot g^{-1}$)[b]	D_p (nm)[b]	Average particle size (nm)[c]
MnO_2-P	206.25	1.34	33.23	26.20
MnO_2-I	49.34	0.10	3.40	70.23
MnO_2-1,2P	205.38	0.95	17.79	35.81
MnO_2-1,3P	218.57	0.88	17.55	82.68
MnO_2-G	194.10	0.38	6.65	20.71

[a] Measured by the BET method.
[b] Measured by the BJH method.
[c] Statistically obtained from SEM images.

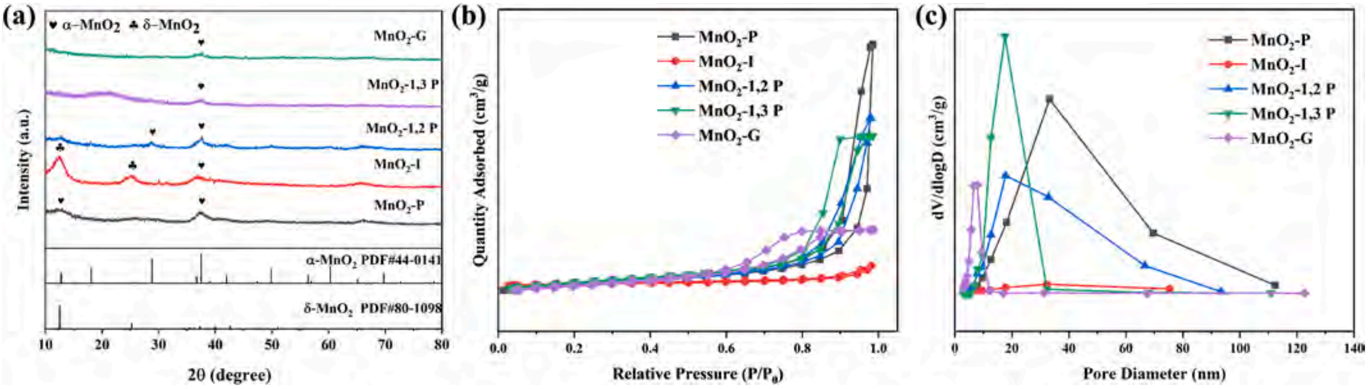

Fig. 1. (a) XRD patterns, (b) N_2 isotherms and (c) corresponding pore size distributions of MnO_2 catalysts prepared by different C_3 alcohols.

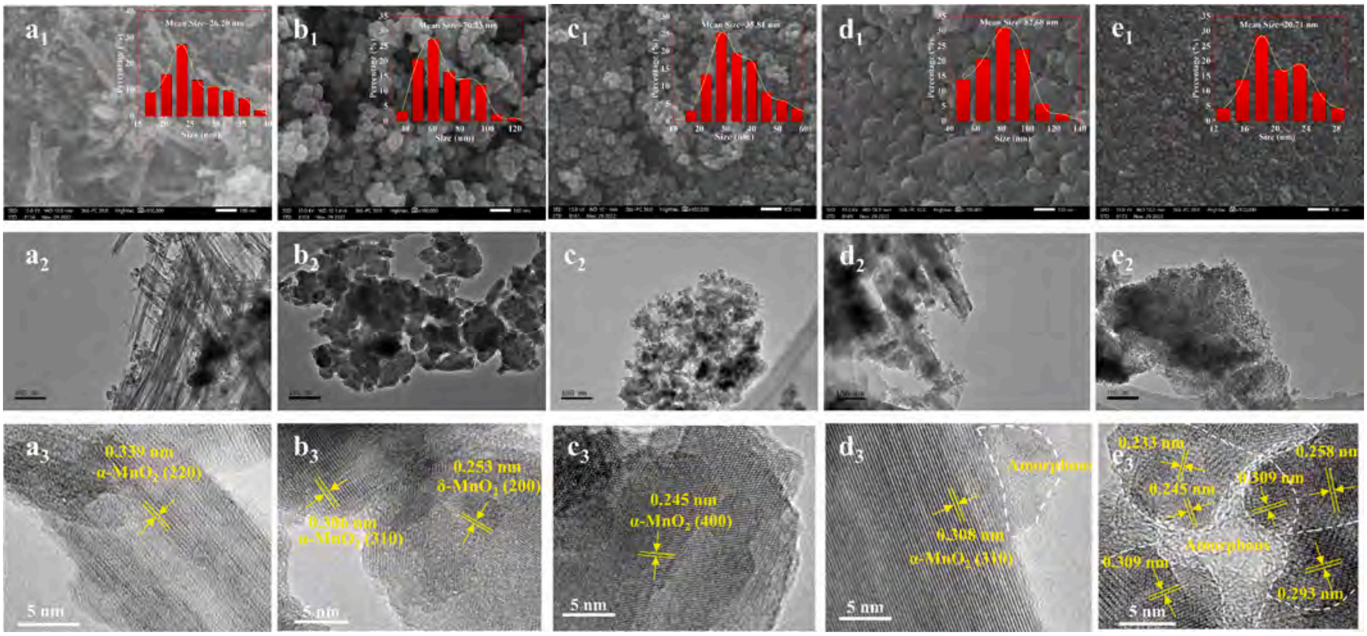

Fig. 2. SEM and TEM images of MnO_2-P (a_1-a_3), MnO_2-I (b_1-b_3), MnO_2-1,2P (c_1-c_3), MnO_2-1,3P (d_1-d_3), MnO_2-G (e_1-e_3).

dense small particles, but its average particle size is as small as 20.71 nm. Additionally, numerous extremely small particles are observed in MnO_2-G from Fig. 2**e₂**. Furthermore, HRTEM reveals the presence of amorphous structures within MnO_2-1,3P and MnO_2-G. However, unlike the amorphous structure present at the edge of MnO_2-1,3P, the amorphous structure of MnO_2-G is surrounded by many microcrystals with different crystal facets, including the (4 0 0) and (3 1 0) crystal planes of α-MnO_2 (0.245, 0.309 nm), the (0 0 3) crystal plane of δ-MnO_2 (0.233 nm), and the (2 0 0) crystal plane of Mn_3O_4 (0.293 nm). The mixed structure rich in microcrystals and amorphous forms of MnO_2-G may contains a large number of grain boundaries, facilitating exposure of more active sites and generation of additional structural defects, thereby enhancing the catalytic activity of MnO_2 [31,35].

3.2. Surface state analysis

The XPS was employed to probe the surface chemical properties and valence states of the synthesized MnO_2 catalysts. In Fig. 3**a**, the convolution peak of Mn $2p_{3/2}$ can be resolved into two peaks, with the peak at 641.9 eV assigned to Mn^{3+}, and the peak at 642.8 eV corresponding to Mn^{4+} [36]. The relative proportions of Mn^{3+} and Mn^{4+} on the surface can be determined based on their respective peak areas, as presented in Table 2. As illustrated in Fig. 3**a**, the surface $Mn^{3+}/(Mn^{3+}+Mn^{4+})$ ratios of different catalysts followed this order: MnO_2-1,3P< MnO_2-P< MnO_2-I< MnO_2-1,2P< MnO_2-G. Additionally, the average valence states of these MnO_2 catalysts were calculated based on the difference in binding energies (ΔEs) corresponding to the double peaks in the Mn 3 s spectra (Fig. 3**b**) [29]. As presented in Table 2, the average oxidation state (AOS) of the synthesized MnO_2 catalysts is 3.35, 3.38, 3.33, 3.60, and 3.10, respectively. The results reveal that the Mn oxidation state is the lowest in the MnO_2-G sample, which can be attributed to the substantial presence of Mn^{3+} on its surface. Moreover, the ICP results in Table 2 showed that the K/Mn of MnO_2-G is notably lower than that of the other MnO_2 samples, which may be attributed to the tunnel collapse caused by the transformation process of α-MnO_2 to an amorphous structure [37]. The overflow of K^+ led to the decrease of the K^+ content in the mixed-crystalline/amorphous MnO_2-G. Since MnO_2-G has the lowest average valence state of Mn and the least amount of K^+, MnO_2-G requires a

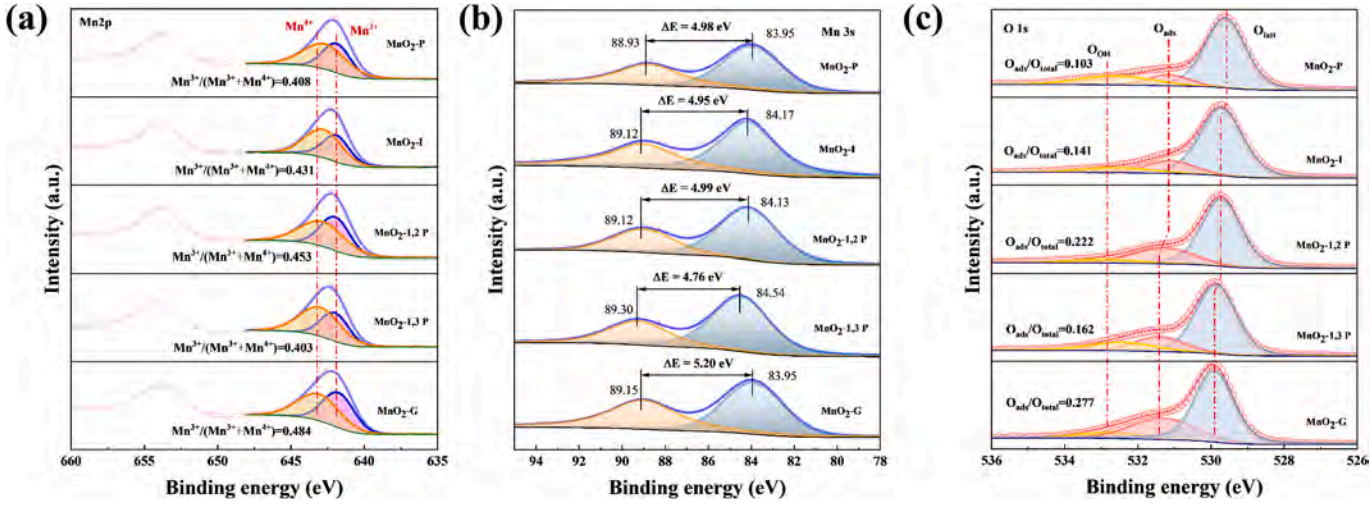

Fig. 3. (a) Mn 2p spectra, (b) Mn 3 s spectra and (c) O 1 s spectra of MnO_2 catalysts prepared by different C_3 alcohols ($O_{total} = O_{OH} + O_{ads} + O_{latt}$).

Table 2
Surface chemical state information and catalytic activities of toluene oxidation over MnO_2 catalysts prepared by different C_3 alcohols.

Catalyst	$Mn^{3+}/(Mn^{3+}+Mn^{4+})$[a]	ΔEs	AOS[b]	O_{ads}/O_{total}[a]	K/Mn[c]	H_2 consumption amount ($mmol\cdot g^{-1}$)[d]	O_2 desorption amount ($mmol\cdot g^{-1}$)[e]
MnO_2-P	0.408	4.98	3.35	0.103	0.302	9.17	1.97
MnO_2-I	0.431	4.95	3.38	0.141	0.415	8.92	1.01
MnO_2-1,2P	0.453	4.99	3.33	0.222	0.176	8.99	2.44
MnO_2-1,3P	0.403	4.76	3.60	0.162	0.151	8.72	2.57
MnO_2-G	0.484	5.20	3.10	0.237	0.022	9.38	2.70

[a] Calculated basing on the relative peak area according to XPS spectra.
[b] Average oxidation state (AOS) was calculated following: AOS = 8.956–1.126ΔEs, where ΔEs represented the difference of binding energies between two Mn 3 s peaks;
[c] Calculated from the ICP results.
[d] The data were estimated by quantitatively analyzing the curves of H_2-TPR.
[e] The data were estimated by quantitatively analyzing the curves of O_2-TPD.

higher concentration of oxygen vacancies to maintain electroneutrality. This was verified by the O 1 s XPS analysis in Fig. 3**c**. Specifically, the O1s asymmetry XPS peak can be divided into three peaks with binding energies positioned at 529.6 eV, 531.15 eV, and 532.6 eV, which correspond to lattice oxygen (O_{latt}), surface adsorbed oxygen (O_{ads}), and surface hydroxyl oxygen (O_{OH}), respectively [24]. In general, an increased quantity of surface oxygen vacancies tends to facilitate the adsorption and activation of gas-phase oxygen, leading to a rise in the content of surface-adsorbed oxygen. [24,38]. According to the quantitative analysis results in Fig. 3**c** and Table 2, MnO_2-G presents the highest O_{ads}/O_{total} compared to other MnO_2 catalysts, indicating that it has the highest oxygen vacancy concentration.

3.3. *Redox properties*

To gain more profound insight into the catalytic oxidation behavior of various MnO_2 catalysts on toluene, the reduction activity and oxygen activity of the samples were evaluated with H_2-TPR and O_2-TPD, respectively. In Fig. 4**a**, the H_2-TPR profile reveals hydrogen uptake occurring below 400 °C for all MnO_2 catalysts. Specifically, weaker peaks below 200 °C are associated with the reduction of surface-adsorbed oxygen [34]. As can be seen in the inset of Fig. 4**a**, MnO_2-G has the largest adsorbed oxygen reduction peak area, which directly indicated the existence of the most chemisorbed oxygen on this Mn-based sample and was consistent with the XPS results. Moreover, the reduction region at 200–400 °C corresponds to the gradual reduction from $Mn^{4+}\rightarrow Mn^{3+}\rightarrow Mn^{2+}$ [34,39]. Similar overlapping reduction peaks of multivalent Mn species can be observed on different Mn-based oxides

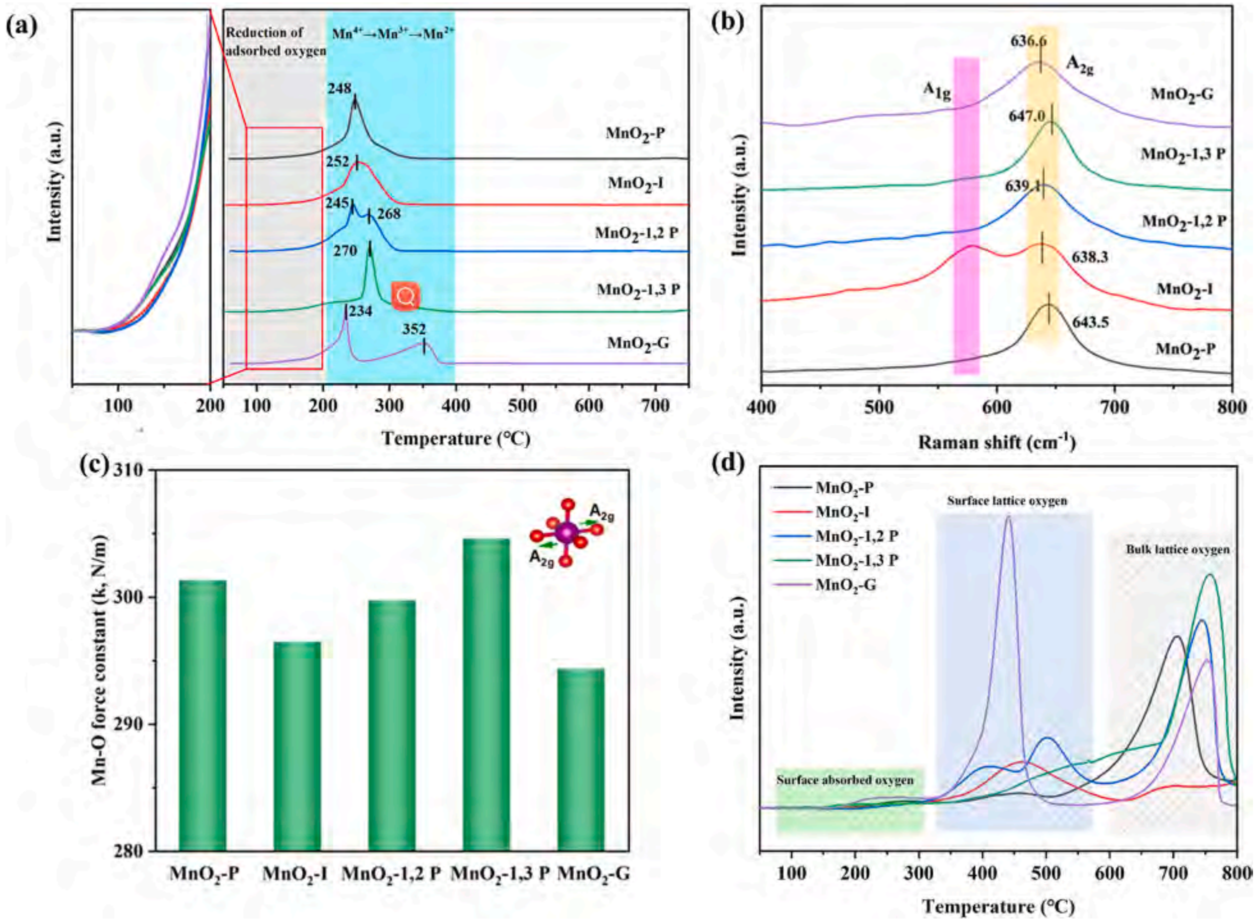

Fig. 4. (a) H_2-TPR, (b) Raman spectra, (c) Mn-O force constant and (d) O_2-TPD of MnO_2 catalysts prepared by different C_3 alcohols.

except MnO_2-G in the range of 200–400 °C, while the main difference lies in the temperature region and intensity of their reduction peaks. In contrast, MnO_2-G displays distinctly separated Mn reduction peaks (234 and 352 °C), and its first reduction peak temperature exhibits a noticeable shift toward lower temperatures compared to other MnO_2. It may be ascribed to the presence of numerous amorphous and microcrystalline complex structures in MnO_2-G, causing a significant weakening of the strength of the six-coordinated Mn-O bonds and rendering them more susceptible to reduction [35]. The structures of these MnO_2 were further examined through Raman spectroscopy, and the corresponding patterns are presented in Fig. 4**b**. The Raman absorption peaks detected at 575 and 625 cm^{-1} corresponded to Mn-O chain stretching vibrations (A_{1g}) and symmetric stretching vibrations of the $[MnO_6]$ group (A_{2g}), respectively [33]. Obviously, the symmetric telescopic vibrational absorption peaks of the $[MnO_6]$ group in MnO_2, prepared from various C_3 alcohols, displayed distinct shifts. Among them, MnO_2-G exhibited a significant blue shift compared to other Mn-based catalysts. The force constant (k) of the Mn-O bond on the material surface can be computed using Hooke's law, represented as follows [38]:

$$\omega = \frac{1}{2\pi c}\sqrt{k/\mu} \tag{5}$$

where ω represents the Raman shift (cm^{-1}), c denotes the speed of light (m/s), and μ is the effective mass (g).

The calculated results revealed a ranking of Mn-O bonding constants for these MnO_2 samples from small to large: MnO_2-G < MnO_2-I < MnO_2-1,2P < MnO_2-P < MnO_2-1,3P, where MnO_2-G exhibited the smallest bonding constant at 294.9 N/m (Fig. 4**c**). This is attributed to the elevated Mn^{3+} content in MnO_2-G, where the strong Jahn-Teller (J-T) effect associated with Mn^{3+} induced elongation of the Mn-O bond in $[MnO_6]$. [38,40]. Combined with the largest hydrogen consumption of MnO_2-G in Table 2, it can be clearly revealed that this catalyst has superior reduction properties compared to MnO_2 synthesized by other C_3 alcohols.

O_2-TPD serves as an effective method for investigating the desorption behavior and activation capacity of diverse oxygen species on the material surface. Generally, the desorption temperature can disclose the presence of different oxygen species on the catalyst surface. As depicted in Fig. 4**d**, three primary oxygen desorption intervals are observed, encompassing desorption peaks below 300 °C (corresponding to surface adsorbed oxygen, both physically and chemically adsorbed oxygen), 300–600 °C (representing surface lattice oxygen), and above 600 °C (indicating bulk phase lattice oxygen) [35]. Between 200 and 300 °C, the oxygen desorption from MnO_2-G is notably higher than that of the

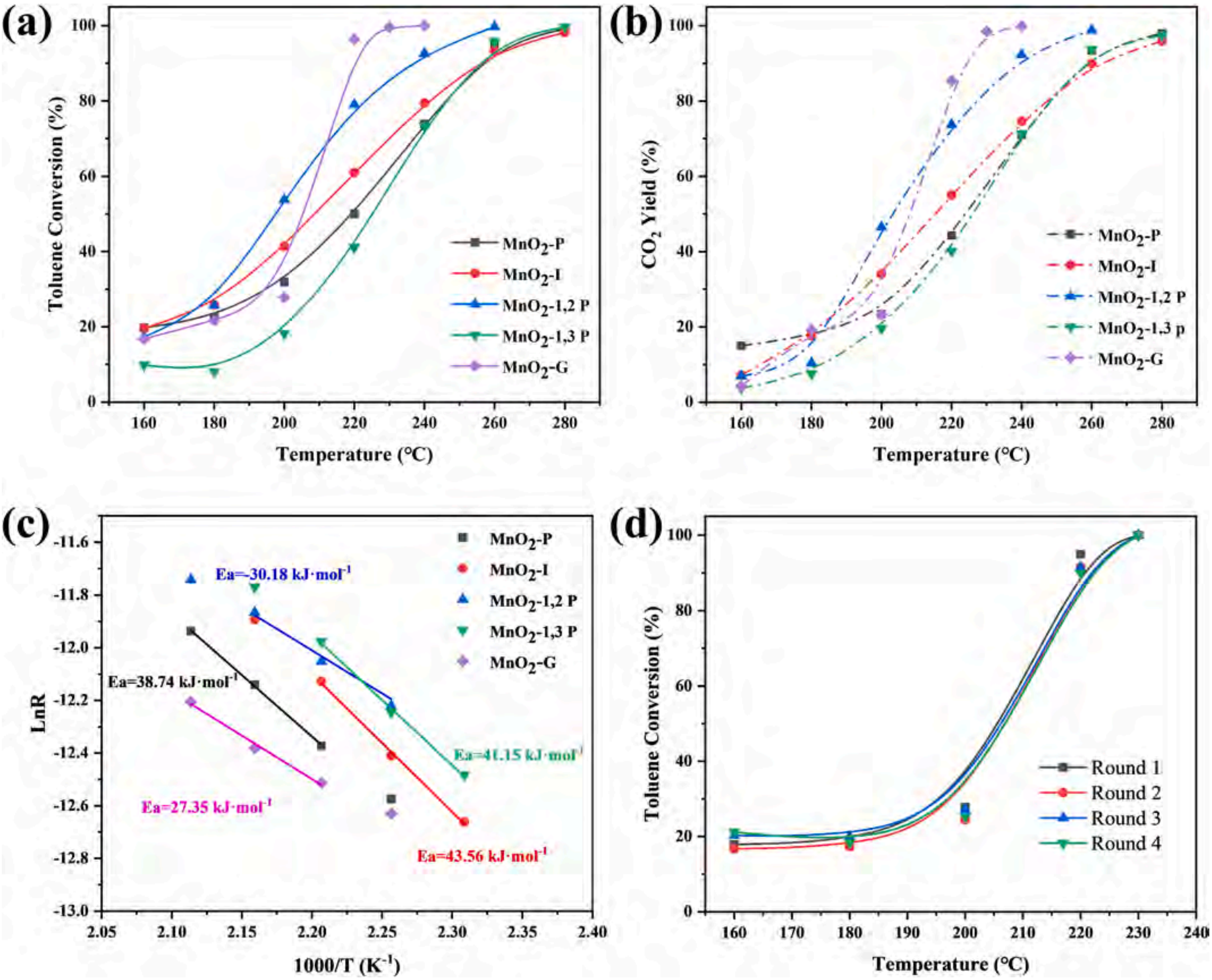

Fig. 5. (a) Toluene conversion, (b) CO_2 yield, (c) Arrhenius plot of MnO_2 catalysts prepared by different C_3 alcohols, (d) cyclic stability of MnO_2-G (Reaction conditions: 600 ppm toluene, 20 % O_2/N_2).

other MnO_2 samples, verifying the conclusion drawn from XPS analysis that MnO_2-G exhibits the highest adsorbed oxygen content. Normally, toluene oxidation obeys the Mars-van Krevelen (MvK) mechanism, where the lattice oxygen activity on the catalyst surface is a key factor influencing catalytic performance [41,42]. The intensity of desorption peaks on MnO_2-G is markedly higher than that on other MnO_2 in the range of 300–600 °C, indicating that the lattice oxygen mobility of MnO_2-G is the highest [33]. According to the TEM characterization results and Raman analysis, it was speculated that the amorphous structure of MnO_2-G weakened the coordination strength between Mn-O, and the microcrystals of MnO_2-G exposed more edge grain boundaries, facilitating the easier activation and desorption of lattice oxygen from the catalyst surface to participate in the oxidation of VOCs [31,43].

3.4. Catalytic performance of toluene oxidation

The results of performance tests for these MnO_2 in the catalytic oxidation of toluene within the temperature range of 160–280 °C are depicted in Fig. 5 **(a-b)**. Under the reaction conditions involving 600 ppm toluene, 20 % oxygen and WHSV = 30,000 $mL \cdot g^{-1} \cdot h^{-1}$, MnO_2-G demonstrated significantly superior catalytic activity in comparison to other MnO_2 catalysts, achieving 96.1 % toluene conversion and 85.6 % CO_2 yield at 220 °C. In contrast, MnO_2-1,2P achieved similar conversion at a higher temperature of 240 °C, and the T_{90} values for MnO_2-P, MnO_2-I, and MnO_2-1,3P are close to 260 °C. The specific catalytic activity and kinetic data are listed in Table 3**.** The toluene oxidation reaction rate of MnO_2-G was 25.81 $\mu mol \cdot g^{-1} \cdot s^{-1}$ at 220 °C, which was higher than that of other MnO_2 catalysts. Moreover, utilizing the data of the catalysts within intervals of less than 20 % toluene conversion at a high weight hourly space velocity of 120,000 $mL \cdot g^{-1} \cdot h^{-1}$, apparent activation energies for toluene oxidation over these prepared MnO_2 catalysts were computed using Arrhenius curves (Fig. 5**c**). The sequential trend of apparent activation energies was as follows: MnO_2-G (27.35 $kJ \cdot mol^{-1}$) < MnO_2-1,2P (30.18 $kJ \cdot mol^{-1}$) < MnO_2-P (38.74 $kJ \cdot mol^{-1}$) < MnO_2-1,3P (41.15 $kJ \cdot mol^{-1}$) < MnO_2-I (43.56 $kJ \cdot mol^{-1}$), indicating MnO_2-G is more favorable for toluene oxidation [27]. Moreover, as depicted in Fig. 5**d**, the toluene conversion displayed excellent reproducibility during all four cycling tests, affirming the superior cycling stability of MnO_2-G. The integration of the above results with SEM, XRD, and TEM analyses revealed that during the redox process, despite the C_3 alcohol acting as the reducing agent having an identical carbon number, distinctions in the position and number of hydroxyl groups induce alterations in the morphology and surface properties of manganese oxides, thus leading to the difference of catalytic properties. Additionally, reports on the catalytic oxidation of toluene by manganese oxides are summarized in **Table S1**. In comparison, the catalytic performance of MnO_2-G (Fig. 5**a** and **Fig. S2**) prepared through the reduction of $KMnO_4$ with glycerol is still competitive.

To validate the applicability of MnO_2-G for the removal of other types of VOCs, chlorobenzene was chosen as a model pollutant to further evaluate the catalytic performance of MnO_2prepared from different C_3 alcohols. Chlorobenzene, as a typical representative of halogenated VOCs, exhibits stronger toxicity and stability compared to toluene and is more prone to causing catalyst poisoning. As depicted in **Fig. S3**, the conversion of chlorobenzene (CB) over MnO_2-P, MnO_2-I, and MnO_2-1,3P did not exceed 40 % even at 400 °C. In contrast, MnO_2-G and MnO_2-1,2P exhibited better CB removal performance. Particularly, MnO_2-G achieved a CB conversion of 87.7 % at 350 °C, surpassing MnO_2-1,2P with a conversion of 60.8 %, consistent with the catalytic activity trend observed for toluene removal. These results demonstrated that MnO_2-G possesses excellent catalytic removal performance for various types of VOCs.

Table 3
Catalytic performance of toluene oxidation over MnO_2 catalysts prepared by different C_3 alcohols.

Catalyst	T_{50} [a] (°C)	T_{90} [a] (°C)	Reaction rate [b] ($\mu mol \cdot g^{-1} \cdot s^{-1}$)	Ea [c] ($kJ \cdot mol^{-1}$)
MnO_2-P	220	257	13.39	38.74
MnO_2-I	209	256	16.33	43.56
MnO_2-1,2P	198	237	21.17	30.18
MnO_2-1,3P	225	254	9.49	41.15
MnO_2-G	205	219	25.81	27.35

[a] Reaction temperatures correspond conversion of toluene at 50 % and 90%.
[b] Reaction rates at 220 °C.
[c] The data were obtained by Arrhenius equation estimation.

3.5. Stability, water resistance, effect of operating conditions, and analysis of application prospects

To evaluate the stability and water resistance of MnO_2-G, the sample was tested for toluene oxidation at a reaction temperature of 225 °C and WHSV of 30,000 $mL \cdot h^{-1} \cdot g^{-1}$. Fig. 6**a** illustrates the results of long-term stability testing for the catalytic oxidation of toluene over MnO_2-G. Within the initial 48 h, the conversion rate of toluene remained essentially unchanged at 100 %, followed by a gradual decline thereafter. Even after 72 h of testing, the toluene conversion was still 91 %, indicating the favorable stability of MnO_2-G. To investigate the reasons behind the decline in catalyst activity, the morphology, crystallinity, and surface chemical state changes of the catalyst before and after use were analyzed using SEM, XRD, and XPS (**Fig. S4-S6**). It can be noticed from **Fig. S4** that the MnO_2-G catalyst retains a microspherical shape after the reaction. However, there was an agglomeration of the grains, which may be due to the sintering of the catalyst. The surface carbon content (**Table S2**) also increased from the original 9.09 % to 13.00 % due to the decrease in catalytic activity leading to the deposition of toluene intermediate products on the catalyst surface. XRD analysis in **Fig. S5** revealed an augmented crystallinity in the reacted MnO_2-G catalyst, with more pronounced crystalline features of α-MnO_2. It may be attributed to the continuous consumption and dynamic replenishment of surface lattice oxygen on MnO_2-G during the oxidation of toluene, leading to a transition from disorder to order in lattice oxygen migration in the amorphous/microcrystalline mixed-phase catalyst. Furthermore, XPS was employed to compare the changes in the chemical states of Mn and O before and after the reaction. As depicted in **Fig. S6**, Mn^{3+}/ (Mn^{3+}+Mn^{4+}) decreased from 0.484 to 0.385. The reduction may be attributed to the intensified activation of adsorbed oxygen by Mn^{3+} during the interaction with O_{ads} and toluene, as represented by the following equation: $Mn^{3+} + O_2^-$ (ads) → $Mn^{4+} + 2O^-$ (ads) [31]. Meanwhile, the proportion of adsorbed oxygen and lattice oxygen decreased from 0.277 and 0.643 before the reaction to 0.212 and 0.579. It indicates that a certain level of depletion in the content of adsorbed oxygen and surface lattice oxygen occurred during the prolonged reaction process, which may be the main reason for the decrease in catalytic activity [38].

Subsequently, the reaction temperature and WHSV were kept constant, and different contents of water vapor (2.5–20 vol%) were introduced into the reaction system to investigate the impact of water concentration on the catalytic performance of MnO_2-G (Fig. 6**b**). Initially, toluene conversion remained essentially unchanged at water contents below 5 vol%. However, as water content increased, toluene conversion gradually declined, with the degree of decrease positively correlating with water content. Notably, even at a higher water content of 20 vol%, toluene conversion remained close to 70 %, which showed that the MnO_2-G had strong resistance to water. Moreover, once stopping the introduction of water vapor, toluene conversion recovered rapidly, indicating the reversible impact of water vapor on toluene.

In general, the operating conditions also affect the catalyst removal performance. Among them, WHSV and initial pollutant concentration are the most important parameters for assessing the usefulness of the

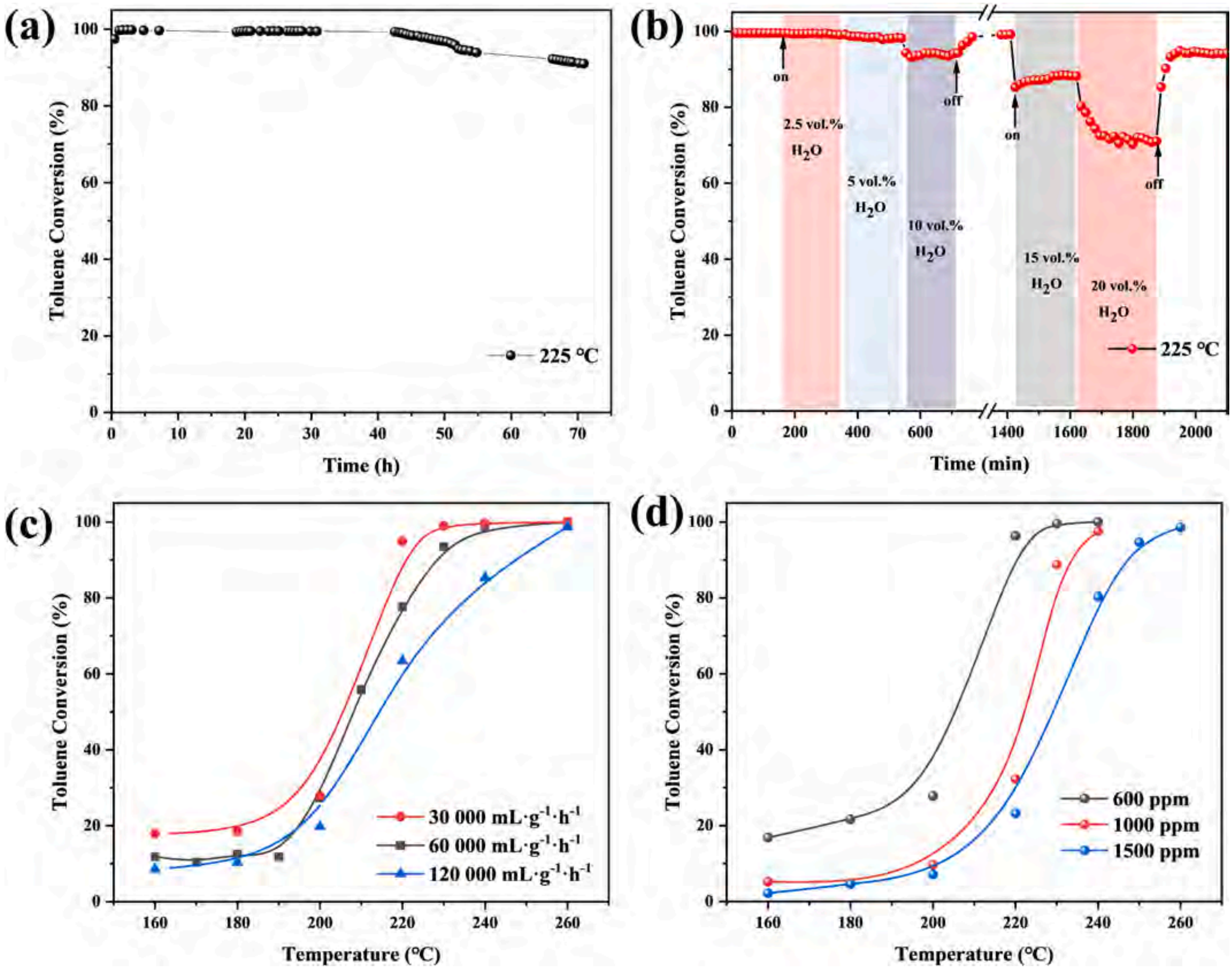

Fig. 6. (a) long-term stability, (b) water resistance, (c-d) the effects of WHSV and initial toluene concentration on the catalytic performance of MnO_2-G.

catalyst. Consequently, the oxidation behavior of toluene over MnO_2-G at different WHSV was further investigated. As depicted in Fig. 6**c**, the toluene conversion gradually decreased with increasing velocity, and the T_{90} for toluene was measured at 219 °C, 228 °C and 247 °C under varying WHSV conditions of 30,000, 60,000, and 120,000 $mL\cdot h^{-1}\cdot g^{-1}$, respectively. The most pronounced decrease in toluene conversion was noted at a WHSV of 120,000 $mL\cdot h^{-1}\cdot g^{-1}$, attributable to the limited contact time between toluene molecules and the finite number of active sites on the MnO_2-G surface. Therefore, in practical application scenarios, the reasonable WHSV is a crucial prerequisite to balance the catalyst performance and economic benefits. Mover, it can be seen from Fig. 6**d** that the toluene removal performance curve of MnO_2-G shifted toward higher temperatures as the pollutant concentration increased. This is because the number of pollutant molecules exceeds the number of active sites on the catalyst surface. At a toluene concentration of 1500 ppm, the T_{90} of MnO_2-G was 247 °C, which was slightly higher than the T_{90} at 1000 ppm (237 °C). Overall MnO_2-G has good operational flexibility and has potential for practical applications.

From the perspective of raw material availability, cost, and potential environmental hazards, the use of glycerol to reduce $KMnO_4$ for the preparation of MnO_2 for VOCs treatment demonstrates promising application potential. Firstly, the crustal abundance of Mn is relatively high and its relative amount of CO_2 produced during mining and purification is quite low [44]. The development of manganese-based catalysts brings significantly smaller environmental impacts than precious metal catalysts. And glycerol is a common chemical raw material with high yield, low price, and easy transportation. Secondly, MnO_2-G is prepared by liquid-phase redox reaction, which is mild and simple and can be used for scale-up with conventional stirred tanks. Thirdly, no toxic gases are generated during the preparation of MnO_2-G, and only CO_2 is generated during the calcination of the precursor. Moreover, the manganese in the production wastewater can be recovered by chemical precipitation and flocculation. Additionally, the deactivated MnO_2 catalysts are recycled as hazardous waste by specialized treatment agencies, with no environmental risk of spillage. Overall, the large-scale preparation of MnO_2-G has low production costs and controllable environmental risks.

3.6. *Catalytic oxidation mechanisms of toluene by in situ DRIFTS*

To investigate the conversion pathways during toluene oxidation, in situ DRIFTS analysis was conducted to monitor the alterations in intermediates on the catalyst surface. In Fig. 7**a**, the IR spectra of MnO_2-G exposed to a toluene/air atmosphere at 50 °C ambient over time revealed gradually enhanced spectral peaks at 1463, 1498, and 1604 cm^{-1}, corresponding to the stretching vibration of C = C bonds in the aromatic ring and the in-plane skeleton vibration [45–48]. The band at 3027 cm^{-1} is the C–H vibration of the benzene ring [49]. Additionally,

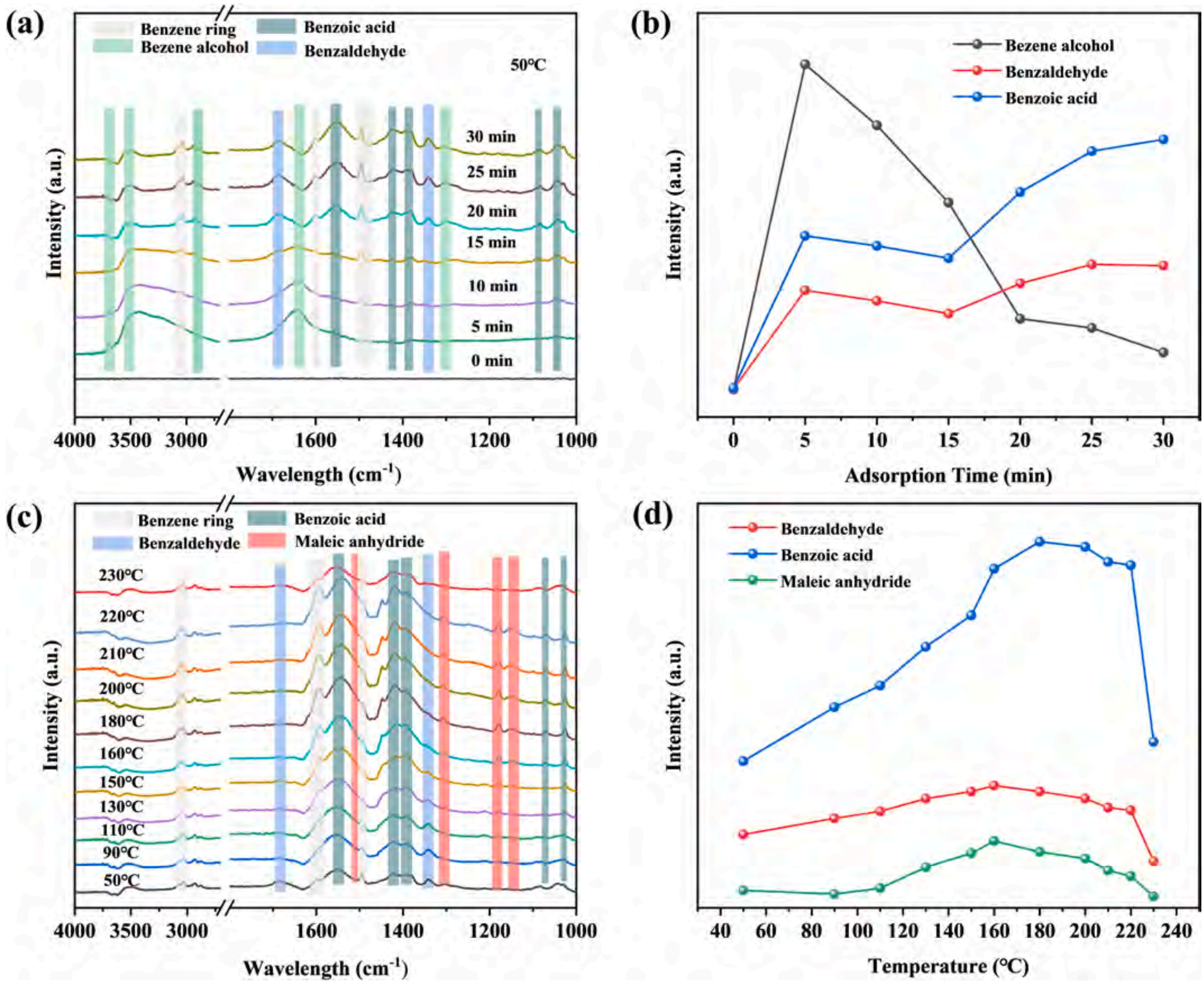

Fig. 7. (a) In situ DRIFTS spectra of toluene absorption on MnO_2-G at 50 °C and (b) the variation of infrared absorption intensity of toluene oxidation intermediates with adsorption time, (c) In situ DRIFTS spectra of toluene oxidation on MnO_2-G at 50–230 °C and (d) the variation of infrared absorption intensity of toluene oxidation intermediates with reaction temperature (600 ppm toluene, air as balanced gas).

two distinct absorption bands at 3545 cm^{-1} and 1639 cm^{-1} represent the stretching vibration of the hydroxyl [O–H] group, while the hydrogen bonding [O···H] stretching vibration is indicated by the band at 3705 cm^{-1} [50–52]. Combined with the typical vibrational peak of C-O at 1279 cm^{-1} and the symmetric and asymmetric C–H stretching vibrations of the [–CH_2-] group at 2878 and 2938 cm^{-1}, it could be hypothesized that toluene adsorbed on the surface of MnO_2-G undergoes rapid conversion to benzyl alcohol [34,49]. It is noteworthy that the intensity of the characteristic peak at 1643 cm^{-1}, representing the benzyl alcohol species, gradually decreases with time until the spectrum disappears at 20 min. Meanwhile, new peaks assigned to the C = O vibration of aldehyde group emerged at 1682 and 1337 cm^{-1} [53,54]. This suggests the gradual conversion of benzyl alcohol to benzaldehyde. Furthermore, the intensity of the two absorption peaks at 1381 and 1551 cm^{-1} gradually increased over time, which were attributed to the symmetric and antisymmetric C = O stretching vibrations of carboxylates, while the characteristic peak at 1421 cm^{-1} is also associated with benzoic acid [45,53]. Therefore, it can be speculated that benzoic acid was also gradually produced during the adsorption of toluene. The changes in the accumulation of toluene oxidation intermediate species (1643 cm^{-1}, benzyl alcohol; 1337 cm^{-1}, benzaldehyde; 1551 cm^{-1}, benzoic acid,) on the catalyst surface with adsorption time were presented in Fig. 7**b**. It is clear that the decrease in benzyl alcohol is accompanied by an increase in benzaldehyde and benzoate. While the intensity of benzaldehyde and benzoate remains relatively stable after 25 min, reaching the adsorption-reaction dynamic equilibrium. It indicates that MnO_2-G can partially oxidize toluene even at low temperatures, possibly due to the high activity of chemisorbed oxygen on the vacancies. **Figures S7(a-b)** showed the infrared spectra of the toluene adsorption process and the accumulation of intermediate products over time for MnO_2-P under 50 °C air atmosphere. During the adsorption process, the characteristic peaks of benzaldehyde and benzoic acid were relatively weak, and their intensities remained essentially unchanged over time, while the accumulation of benzyl alcohol increased significantly over time. It indicated that compared to MnO_2-G, the catalytic oxidation ability of MnO_2-P towards toluene was limited, and insufficient to oxidize benzyl alcohol to benzaldehyde and benzoic acid at low temperatures. This may be related to the fact that MnO_2-P has fewer adsorbed oxygen species.

Moreover, the transformation of toluene oxidation on the MnO_2-G and MnO_2-P surfaces at different temperatures was further investigated by heating the in situ cell while maintaining a continuous passage of toluene/air. As depicted in Fig. 7**c**, the intensity of benzaldehyde and benzoic acid progressively increased with rising temperature, accompanied by the appearance of characteristic signals associated with maleic anhydride (1305 cm^{-1}, 1180 cm^{-1}, 1141 cm^{-1}) [55,56]. The observation implied that elevated temperature facilitated the conversion of toluene into benzaldehyde and benzoic acid as well as the formation of maleic anhydride through deep oxidative ring-opening reactions. Similarly, the accumulation of benzaldehyde, benzoic acid, and maleic anhydride as a function of temperature was exhibited in Fig. 7**d**. Notably, benzoic acid predominates among these substances, indicating that the ring-opening reaction of benzoic acid is the most thermodynamically challenging and thus represents the rate-limiting step in toluene oxidation. The conclusion is consistent with numerous reports in the existing literature [45,57]. Additionally, the infrared signals corresponding to these three intermediate species exhibited an initial increase and subsequent decrease with increasing temperature, experiencing a sharp decline beyond 220 °C. At 230 °C, the accumulated amount of these species on the catalyst surface was lower than the initial value observed at 50 °C, suggesting the complete transformation of intermediates. This phenomenon can be attributed to the activation of surface lattice oxygen at elevated temperatures, facilitating its participation in toluene oxidation. The depletion of lattice oxygen is swiftly replenished by substantial gaseous oxygen, thus establishing an efficient oxygen cycle that ensures the sustained and thorough oxidation of toluene. However, it could be seen from **Fig. S7**(c-d) that the signal intensity of toluene oxidation intermediates on the surface of MnO_2-P is continuously increasing with temperature. It indicated that the accumulation rate of intermediate products exceeded the decomposition rate in the range of 50–250 °C, which proved that the activity of lattice oxygen in crystalline MnO_2-P was weaker than that of MnO_2-G under the same conditions.

Isotopic labeling experiments ($^{18}O_2$-TPSR) were employed to further investigate the changes in oxygen species involved in the toluene oxidation reaction, as depicted in **Fig. S8**. The signal of $C^{18}O$ was observed even at 100 °C, indicating the involvement of gaseous $^{18}O_2$ in the reaction. Since surface-adsorbed oxygen was removed during sample pretreatment, the oxygen species in $C^{18}O$ can only originate from gaseous $^{18}O_2$. It suggests that the oxygen vacancies of MnO_2-G can adsorb and activate $^{18}O_2$ to generate the reactive adsorbed oxygen species to partially oxidize toluene. As the temperature increased, a distinct peak corresponding to $C^{16}O_2$ emerged, in which ^{16}O came from surface lattice oxygen. This indicates that at elevated temperatures, surface lattice oxygen can desorb from the catalyst surface to participate in the toluene oxidation process. Furthermore, the generation of $C^{18}O^{16}O$ can be observed at higher temperatures, which may be because the original surface lattice oxygen ^{16}O of MnO_2-G was partially consumed and then replenished by $^{18}O_2$, resulting in the simultaneous presence of ^{16}O and ^{18}O on the catalyst surface.

Based on the preceding analysis and insights from existing literature, a possible reaction mechanism occurring on the surface of MnO_2-G was proposed, as depicted in Fig. 8. Specifically, the presence of numerous grain boundaries and unsaturated coordinating bonds in MnO_2-G facilitates oxygen adsorption and activation, resulting in the formation of highly active adsorbed state oxygen. Simultaneously, the Jahn-Teller effect induced by Mn^{3+} weakens the strength of Mn-O bonds, enhancing the reactivity of surface lattice oxygen. Consequently, the adsorbed oxygen and the surface-active lattice oxygen of MnO_2-G synergistically engage in the catalytic oxidation of toluene molecules at lower temperatures. This oxidation process follows the sequential transformation of toluene → benzyl alcohol → benzaldehyde → benzoic acid → maleic anhydride, ultimately mineralizing into CO_2 and water. Furthermore, the rapid replenishment of gaseous oxygen effectively restores depleted lattice oxygen at the amorphous/crystalline interface, ensuring the continuation of the reaction cycle.

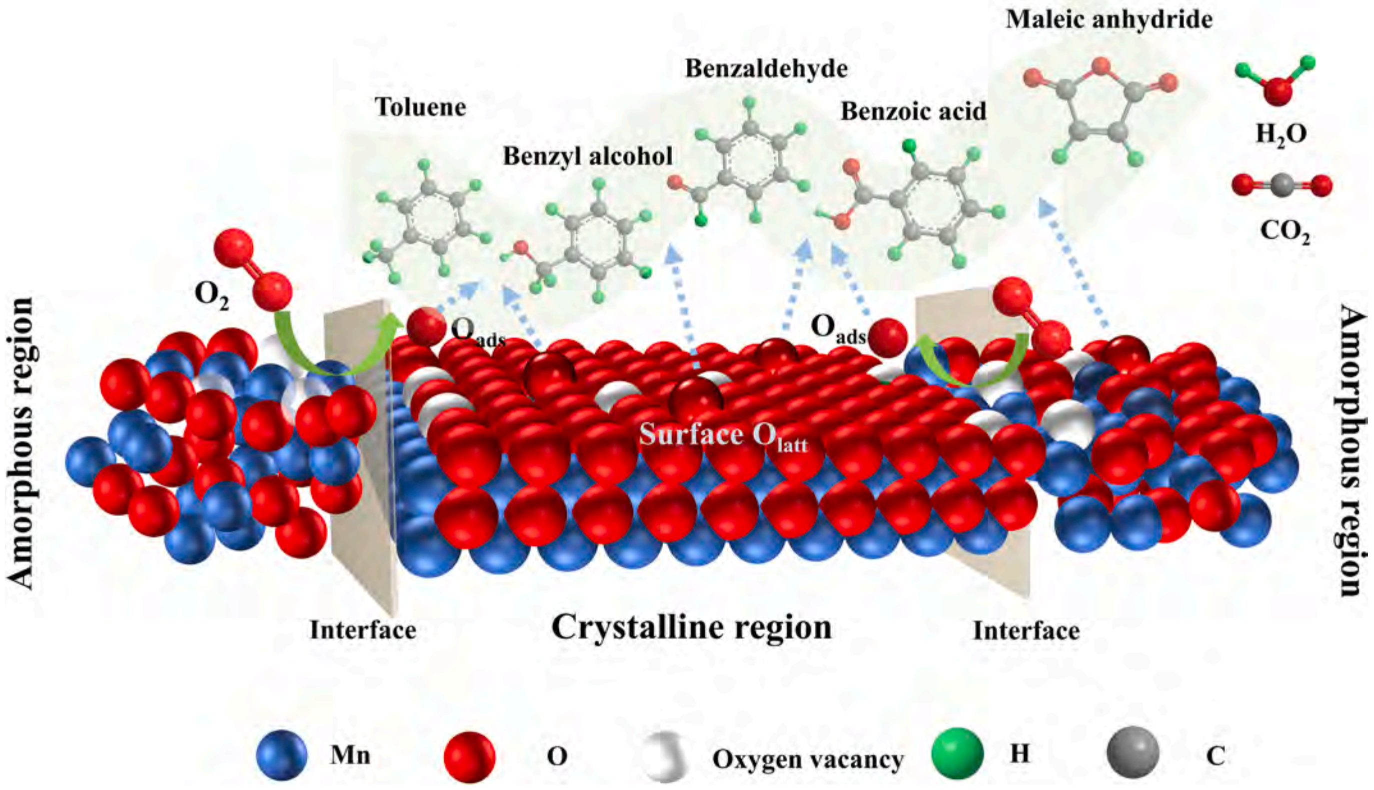

Fig. 8. Schematic of the possible reaction mechanism of toluene oxidation over MnO_2-G catalysts.

4. Conclusion

In summary, this study successfully synthesized a series of novel manganese oxide catalysts through the reduction of C_3 alcohols employing potassium permanganate. Comparative assessments of these catalysts indicated that the MnO_2-G derived from glycerol exhibited a substantially heightened catalytic performance in the toluene and chlorobenzene oxidation compared to MnO_2 obtained from mono- and diols of C_3 alcohols. The superior catalytic performance of MnO_2-G can be ascribed to various factors. Firstly, the MnO_2-G surface features a combination of amorphous and microcrystalline crystalline phases, leading to an increase in phase interfaces. Moreover, the presence of asymmetric coordination structures in the amorphous phase makes the catalyst more susceptible to the formation of surface defects, thus promoting oxygen adsorption and activation. Furthermore, the superior reducibility of glycerol, compared to other C_3 alcohols, results in an increased Mn^{3+} content on the MnO_2-G surface, elongating Mn-O bonds and enhancing the mobility of surface lattice oxygen. Overall, the collaborative effects of these factors enable the effective oxidation of toluene and intermediate molecules by the electrophilic oxygen adsorbed on the surface and the surface-active lattice oxygen on the MnO_2-G catalyst. Additionally, in situ infrared characterization revealed the intermediates' transfer pathway during toluene oxidation on MnO_2-G. This study offers valuable insights into the low-cost development of highly efficient manganese-based oxide catalysts for the oxidation of VOCs.

CRediT authorship contribution statement

Jungang Zhao: Writing – original draft, Visualization, Software, Methodology, Investigation, Formal analysis, Data curation, Conceptualization. **Caiting Li:** Conceptualization, Supervision, Validation. **Xuan Liu:** Supervision, Writing – review & editing. **Shanhong Li:** Software, Writing – review & editing. **Youcai Zhu:** Writing – review & editing. **Le Huang:** Writing – review & editing. **Kuang Yang:** Writing – review & editing. **Ziang Zhang:** Writing – review & editing. **Ying Zhang:** Writing – review & editing. **Qi Huang:** Writing – review & editing.

Declaration of competing interest

The authors declare that they have no known competing financial interests or personal relationships that could have appeared to influence the work reported in this paper.

Data availability

Data will be made available on request.

Acknowledgements

This work was financially supported by National Natural Science Foundation of China (52270102, 52300159) and Natural Science Foundation of Hunan Province (2022JJ40071).

Appendix A. Supplementary material

Supplementary data to this article can be found online at https://doi.org/10.1016/j.seppur.2024.127348.

References

[1] M.S. Kamal, S.A. Razzak, M.M. Hossain, Catalytic oxidation of volatile organic compounds (VOCs)-A review, Atmos. Environ. 140 (2016) 117–134, https://doi.org/10.1016/j.atmosenv.2016.05.031.

[2] I. Lehmann, A. Thoelke, M. Rehwagen, U. Rolle-Kampczyk, U. Schlink, R. Schulz, M. Borte, U. Diez, O. Herbarth, The influence of maternal exposure to volatile organic compounds on the cytokine secretion profile of neonatal T cells, Environ. Toxicol. 17 (3) (2002) 203–210, https://doi.org/10.1002/tox.10055.

[3] V. Hequet, C. Raillard, O. Debono, F. Thévenet, N. Locoge, L. Le Coq, Photocatalytic oxidation of VOCs at ppb level using a closed-loop reactor: the mixture effect, Appl. Catal., B 226 (2018) 473–486, https://doi.org/10.1016/j.apcatb.2017.12.041.

[4] Y. Yang, H. Luo, R. Liu, G. Li, Y. Yu, T. An, The exposure risk of typical VOCs to the human beings via inhalation based on the respiratory deposition rates by proton transfer reaction-time of flight-mass spectrometer, Ecotoxicol. Environ. Saf. 197 (2020) 110615, https://doi.org/10.1016/j.ecoenv.2020.110615.

[5] J. Zhao, C. Li, X. Du, Y. Zhu, S. Li, X. Liu, C. Liang, Q. Yu, L. Huang, K. Yang, Recent progress of carbon dots for air pollutants detection and photocatalytic removal: synthesis, modifications, and applications, Small 18 (51) (2022) 2200744, https://doi.org/10.1002/smll.202200744.

[6] H.-H. Yang, S.K. Gupta, N.B. Dhital, L.-C. Wang, S.P. Elumalai, Comparative investigation of coal-and oil-fired boilers based on emission factors, ozone and secondary organic aerosol formation potentials of VOCs, J. Environ. Sci. 92 (2020) 245–255, https://doi.org/10.1016/j.jes.2020.02.024.

[7] K. Wu, X. Yang, D. Chen, S. Gu, Y. Lu, Q. Jiang, K. Wang, Y. Ou, Y. Qian, P. Shao, Estimation of biogenic VOC emissions and their corresponding impact on ozone and secondary organic aerosol formation in China, Atmos. Res. 231 (2020) 104656, https://doi.org/10.1016/j.atmosres.2019.104656.

[8] R. Peng, S. Li, X. Sun, Q. Ren, L. Chen, M. Fu, J. Wu, D. Ye, Size effect of Pt nanoparticles on the catalytic oxidation of toluene over Pt/CeO_2 catalysts, Appl. Catal., B 220 (2018) 462–470, https://doi.org/10.1016/j.apcatb.2017.07.048.

[9] B. Wang, B. Chen, Y. Sun, H. Xiao, X. Xu, M. Fu, J. Wu, L. Chen, D. Ye, Effects of dielectric barrier discharge plasma on the catalytic activity of Pt/CeO_2 catalysts, Appl. Catal., B 238 (2018) 328–338, https://doi.org/10.1016/j.apcatb.2018.07.044.

[10] Y. Zhu, C. Li, C. Liang, S. Li, X. Liu, X. Du, K. Yang, J. Zhao, Q. Yu, Y. Zhai, Regulating CeO_2 morphologies on the catalytic oxidation of toluene at lower temperature: a study of the structure-activity relationship, J. Catal. 418 (2023) 151–162, https://doi.org/10.1016/j.jcat.2023.01.012.

[11] T. Dong, J. Ji, L. Yu, P. Huang, Y. Li, Z. Suo, B. Liu, Z. Hu, H. Huang, Tunable interfacial electronic Pd–Si interaction boosts catalysis via accelerating O_2 and H_2O activation, JACS Au 3 (4) (2023) 1230–1240, https://doi.org/10.1021/jacsau.3c00093.

[12] P. Gong, F. He, J. Xie, D. Fang, Catalytic removal of toluene using MnO_2-based catalysts: A review, Chemosphere 318 (2023) 137938, https://doi.org/10.1016/j.chemosphere.2023.137938.

[13] M. Xiao, X. Yu, Y. Guo, M. Ge, Boosting toluene combustion by tuning electronic metal-support interactions in in situ grown Pt@Co_3O_4 catalysts, Environ. Sci. Technol. 56 (2) (2022) 1376–1385, https://doi.org/10.1021/acs.est.1c07016.

[14] J. Shi, T. Qi, B.C. Sun, G.W. Chu, J.F. Chen, Catalytic oxidation of benzyl alcohol over MnO_2: Structure-activity description and reaction mechanism, Chem. Eng. J. 440 (2022), https://doi.org/10.1016/j.cej.2022.135802.

[15] C. He, J. Cheng, X. Zhang, M. Douthwaite, S. Pattisson, Z. Hao, Recent advances in the catalytic oxidation of volatile organic compounds: A review based on pollutant sorts and sources, Chem. Rev. 119 (7) (2019) 4471–4568, https://doi.org/10.1021/acs.chemrev.8b00408.

[16] H. Liu, J. Chen, Y. Wang, R. Yin, W. Yang, G. Wang, W. Si, Y. Peng, J. Li, Interaction mechanism for simultaneous elimination of nitrogen oxides and toluene over the bifunctional CeO_2-TiO_2 mixed oxide catalyst, Environ. Sci. Technol. 56 (7) (2022) 4467–4476, https://doi.org/10.1021/acs.est.1c08424.

[17] Y. Li, T. Chen, S. Zhao, P. Wu, Y. Chong, A. Li, Y. Zhao, G. Chen, X. Jin, Y. Qiu, D. Ye, Engineering cobalt oxide with coexisting cobalt defects and oxygen vacancies for enhanced catalytic oxidation of toluene, ACS Catal. 12 (9) (2022) 4906–4917, https://doi.org/10.1021/acscatal.2c00296.

[18] C. Wang, J. Chen, Q. Li, S. Su, H. Jia, H. He, Unveiling the position effect of ce within layered MnO_2 to prolong the ambient removal of indoor HCHO, Environ. Sci. Technol. 57 (2023) 4598–4607, https://doi.org/10.1021/acs.est.3c00420.

[19] X. Liang, L. Wang, T. Wen, H. Liu, J. Zhang, Z. Liu, C. Zhu, C. Long, Mesoporous poorly crystalline alpha-Fe_2O_3 with abundant oxygen vacancies and acid sites for ozone decomposition, Sci. Total Environ. 804 (2022) 150161, https://doi.org/10.1016/j.scitotenv.2021.150161.

[20] R. Tian, H. Dong, J. Chen, R. Li, Q. Xie, Amorphous Co_3O_4 nanoparticles-decorated biochar as an efficient activator of peroxymonosulfate for the removal of sulfamethazine in aqueous solution, Sep. Purif. Technol. 250 (2020) 117246, https://doi.org/10.1016/j.seppur.2020.117246.

[21] M. Kim, G. Park, H. Lee, Local structure and redox properties of amorphous CeO_2-TiO_2 prepared using the H_2O_2-modified sol-gel method, Nanomaterials 11 (8) (2021) 2148, https://doi.org/10.3390/nano11082148.

[22] Y. Bai, Y. Hou, Q. Li, X. Han, H. Wang, Z. Wu, Z. Huang, Amorphous FeO_x-$Mn_{0.1}O_y$ catalyst with rich oxygen vacancies for ammonia selective catalytic reduction of nitrogen oxide at low temperatures, Fuel 349 (2023) 128644, https://doi.org/10.1016/j.fuel.2023.128644.

[23] R. Yang, Y. Fan, R. Ye, Y. Tang, X. Cao, Z. Yin, Z. Zeng, MnO2-based materials for environmental applications, Adv. Mater. 33 (9) (2021) 2004862, https://doi.org/10.1002/adma.202004862.

[24] S. Wu, H. Liu, Z. Huang, H. Xu, W. Shen, O-vacancy-rich porous MnO_2 nanosheets as highly efficient catalysts for propane catalytic oxidation, Appl. Catal., B 312 (2022) 121387, https://doi.org/10.1016/j.apcatb.2022.121387.

[25] Y. Lyu, C. Li, X. Du, Y. Zhu, Y. Zhang, S. Li, Catalytic oxidation of toluene over MnO2 catalysts with different Mn (II) precursors and the study of reaction pathway, Fuel 262 (2020) 116610, https://doi.org/10.1016/j.fuel.2019.116610.

[26] P. Wu, X. Jin, Y. Qiu, D. Ye, Recent progress of thermocatalytic and photo/thermocatalytic oxidation for VOCs purification over manganese-based oxide catalysts, Environ. Sci. Technol. 55 (8) (2021) 4268–4286, https://doi.org/10.1021/acs.est.0c08179.

[27] W. Yang, Z. a. Su, Z. Xu, W. Yang, Y. Peng and J. Li, Comparative study of alpha-, beta-, gamma- and delta-MnO_2 on toluene oxidation: Oxygen vacancies and reaction intermediates, Appl. Catal., B 260 (2020) 118150. DOI: 10.1016/j.apcatb.2019.118150.

[28] R. Yang, Y. Fan, R. Ye, Y. Tang, X. Cao, Z. Yin, Z. Zeng, MnO_2 -based materials for environmental applications, Adv. Mater. 33 (9) (2021) e2004862.

[29] Y. Wen, Y. Zhang, L. He, H. Li, Z. Zhuang, Y. Yu, Activating lattice oxygen in amorphous MnO_2 nanostructure for efficiently selective aerobic oxidation of 5-hydroxymethylfurfural to 2,5-furandicarboxylic acid, ACS Appl. Nano Mater. 5 (8) (2022) 11559–11566, https://doi.org/10.1021/acsanm.2c02478.

[30] Y. Gao, Z. Wang, C. Cui, B. Wang, W. Liu, W. Liu, L. Wang, Amorphous manganese oxide as highly active catalyst for soot oxidation, Environ. Sci. Pollut. Res. 27 (2020) 13488–13500, https://doi.org/10.1007/s11356-020-07909-y.

[31] L. Zhou, B. Zhang, Z. Li, X. Zhang, R. Liu, J. Yun, Amorphous-microcrystal combined manganese oxides for efficiently catalytic combustion of VOCs, Mol. Catal. 489 (2020) 110920, https://doi.org/10.1016/j.mcat.2020.110920.

[32] H. Zhang, J. Wang, Y. Zhang, Y. Jiao, C. Ren, M. Gong and Y. Chen, A study on H_2-TPR of $Pt/Ce_{0.27}Zr_{0.73}O_2$ and $Pt/Ce_{0.27}Zr_{0.70}La_{0.03}O_x$ for soot oxidation, Appl. Surf. Sci. 377 (2016) 48-55. DOI: 10.1016/j.apsusc.2016.03.102.

[33] Y. Yu, S. Liu, J. Ji, H. Huang, Amorphous MnO_2 surviving calcination: an efficient catalyst for ozone decomposition, Cat. Sci. Technol. 9 (18) (2019) 5090–5099, https://doi.org/10.1039/c9cy01426h.

[34] S. Mo, Q. Zhang, J. Li, Y. Sun, Q. Ren, S. Zou, Q. Zhang, J. Lu, M. Fu, D. Mo, Highly efficient mesoporous MnO_2 catalysts for the total toluene oxidation: Oxygen-vacancy defect engineering and involved intermediates using in situ DRIFTS, Appl. Catal., B 264 (2020) 118464, https://doi.org/10.1016/j.apcatb.2019.118464.

[35] Q. Cheng, Z. Yang, Y. Li, J. Wang, J. Wang, G. Zhang, Amorphous/crystalline $Cu_{1.5}Mn_{1.5}O_4$ with rich oxygen vacancies for efficiently photothermocatalytic mineralization of toluene, Chem. Eng. J. 471 (2023) 144295, https://doi.org/10.1016/j.cej.2023.144295.

[36] P. Wu, S. Dai, G. Chen, S. Zhao, Z. Xu, M. Fu, P. Chen, Q. Chen, X. Jin, Y. Qiu, S. Yang, D. Ye, Interfacial effects in hierarchically porous α-MnO_2/Mn_3O_4 heterostructures promote photocatalytic oxidation activity, Appl. Catal., B 268 (2020) 118418, https://doi.org/10.1016/j.apcatb.2019.118418.

[37] S. Rong, K. Li, P. Zhang, F. Liu, J. Zhang, Potassium associated manganese vacancy in birnessite-type manganese dioxide for airborne formaldehyde oxidation, Cat. Sci. Technol. 8 (7) (2018) 1799–1812, https://doi.org/10.1039/c7cy02121f.

[38] J. Zeng, H. Xie, H. Zhang, M. Huang, X. Liu, G. Zhou, Y. Jiang, Insight into the effects of oxygen vacancy on the toluene oxidation over alpha-MnO_2 catalyst, Chemosphere 291 (2022) 132890, https://doi.org/10.1016/j.chemosphere.2021.132890.

[39] L. Zhao, Z. Zhang, Y. Li, X. Leng, T. Zhang, F. Yuan, X. Niu, Y. Zhu, Synthesis of Ce_aMnO_x hollow microsphere with hierarchical structure and its excellent catalytic performance for toluene combustion, Appl. Catal., B 245 (2019) 502–512, https://doi.org/10.1016/j.apcatb.2019.01.005.

[40] W. Yang, Y. Zhu, F. You, L. Yan, Y. Ma, C. Lu, P. Gao, Q. Hao, W. Li, Insights into the surface-defect dependence of molecular oxygen activation over birnessite-type MnO_2, Appl. Catal., B 233 (2018) 184–193, https://doi.org/10.1016/j.apcatb.2018.03.107.

[41] M. Zhang, G. Li, Q. Li, J. Chen, E.A. Elimian, H. Jia, H. He, In situ construction of manganese oxide photothermocatalysts for the deep removal of toluene by highly utilizing sunlight energy, Environ. Sci. Technol. 57 (2023) 4286–4297, https://doi.org/10.1021/acs.est.2c09136.

[42] Y. Ren, X. Lei, H. Wang, J. Xiao, Z. Qu, Enhanced catalytic performance of la-doped $CoMn_2O_4$ catalysts by regulating oxygen species activity for VOCs oxidation, ACS Catal. 12 (2023) 8293–8306, https://doi.org/10.1021/acscatal.3c01036.

[43] X. Li, M. Chen, G. Li, P. Wang, Constructing MnO_2 alpha/amorphous heterophase junction by mechanochemically induced phase transformation for formaldehyde oxidation, Appl. Surf. Sci. 589 (2022) 152855, https://doi.org/10.1016/j.apsusc.2022.152855.

[44] S. Thampy, N. Ashburn, K. Cho, J.W.P. Hsu, Earth-abundant transition metal-based mullite-type oxide catalysts for heterogeneous oxidation reactions, Adv. Energy Sustain. Res. 2 (4) (2021), https://doi.org/10.1002/aesr.202000075.

[45] P. Wang, J. Wang, X. An, J. Shi, W. Shangguan, X. Hao, G. Xu, B. Tang, A. Abudula, G. Guan, Generation of abundant defects in Mn-Co mixed oxides by a facile agar-gel method for highly efficient catalysis of total toluene oxidation, Appl. Catal., B 282 (2021) 119560, https://doi.org/10.1016/j.apcatb.2020.119560.

[46] S. Mo, Q. Zhang, Y. Sun, M. Zhang, J. Li, Q. Ren, M. Fu, J. Wu, L. Chen, D. Ye, Gaseous CO and toluene co-oxidation over monolithic core–shell Co_3O_4-based hetero-structured catalysts, J. Mater. Chem. A 7 (27) (2019) 16197–16210, https://doi.org/10.1039/C9TA03750K.

[47] J. Zhao, C. Li, Q. Yu, Y. Zhu, X. Liu, S. Li, C. Liang, Y. Zhang, L. Huang, K. Yang, Interface engineering of Mn_3O_4/Co_3O_4 S-scheme heterojunctions to enhance the photothermal catalytic degradation of toluene, J. Hazard. Mater. 452 (2023) 131249, https://doi.org/10.1016/j.jhazmat.2023.131249.

[48] J.J. Li, E.Q. Yu, S.C. Cai, X. Chen, J. Chen, H.P. Jia, Y. j., Xu, Noble metal free, CeO_2/$LaMnO_3$ hybrid achieving efficient photo-thermal catalytic decomposition of volatile organic compounds under IR light, Appl. Catal., B 240 (2019) 141–152, https://doi.org/10.1016/j.apcatb.2018.08.069.

[49] H. Gao, X. Lv, M. Zhang, Q. Li, J. Chen, Z. Hu, H. Jia, Copper-cobalt strong interaction to improve photothermocatalytic performance of cobalt-copper oxides supported on copper foam for toluene oxidation, Chem. Eng. J. 434 (2022) 134618, https://doi.org/10.1016/j.cej.2022.134618.

[50] H. Zhang, X. Zheng, T. Xu, P. Zhang, Atomically dispersed Y or La on birnessite-type MnO_2 for the catalytic decomposition of low-concentration toluene at room temperature, ACS Appl. Mater. Interfaces 13 (15) (2021) 17532–17542, https://doi.org/10.1021/acsami.1c01433.

[51] H. Zhang, S. Sui, X. Zheng, R. Cao, P. Zhang, One-pot synthesis of atomically dispersed Pt on MnO_2 for efficient catalytic decomposition of toluene at low temperatures, Appl. Catal., B 257 (2019) 117878, https://doi.org/10.1016/j.apcatb.2019.117878.

[52] L.C. Chen, G.T. Pan, T.C.K. Yang, T.W. Chung, C.M. Huang, In situ DRIFT and kinetic studies of photocatalytic degradation on benzene vapor with visible-light-driven silver vanadates, J. Hazard. Mater. 178 (1) (2010) 644–651, https://doi.org/10.1016/j.jhazmat.2010.01.133.

[53] M. Zhang, S. Cai, J. Li, E.A. Elimian, J. Chen, H. Jia, Ternary multifunctional catalysts of polymeric carbon nitride coupled with Pt-embedded transition metal oxide to enhance light-driven photothermal catalytic degradation of VOCs, J. Hazard. Mater. 412 (2021) 125266, https://doi.org/10.1016/j.jhazmat.2021.125266.

[54] C. Dong, Z. Qu, Y. Qin, Q. Fu, H. Sun, X. Duan, Revealing the highly catalytic performance of spinel $CoMn_2O_4$ for toluene oxidation: Involvement and replenishment of oxygen species using in situ designed-TP techniques, ACS Catal. 9 (8) (2019) 6698–6710, https://doi.org/10.1021/acscatal.9b01324.

[55] J. Wang, X. Wang, X. Liu, J. Zeng, Y. Guo, T. Zhu, Kinetics and mechanism study on catalytic oxidation of chlorobenzene over V_2O_5/TiO_2 catalysts, J. Mol. Catal. A: Chem. 402 (2015) 1–9, https://doi.org/10.1016/j.molcata.2015.03.003.

[56] J. Wang, X. Wang, X. Liu, T. Zhu, Y. Guo, H. Qi, Catalytic oxidation of chlorinated benzenes over V_2O_5/TiO_2 catalysts: The effects of chlorine substituents, Catal. Today 241 (2015) 92–99, https://doi.org/10.1016/j.cattod.2014.04.002.

[57] X. Zhang, F. Bi, Z. Zhu, Y. Yang, S. Zhao, J. Chen, X. Lv, Y. Wang, J. Xu, N. Liu, The promoting effect of H_2O on rod-like $MnCeO_x$ derived from MOFs for toluene oxidation: A combined experimental and theoretical investigation, Appl. Catal., B 297 (2021) 120393, https://doi.org/10.1016/j.apcatb.2021.120393.